

Lab on a Chip

Devices and applications at the micro- and nanoscale

Accepted Manuscript

This article can be cited before page numbers have been issued, to do this please use: M. J. Rasna and J. C. Sturm, *Lab Chip*, 2026, DOI: 10.1039/D5LC00786K.



This is an Accepted Manuscript, which has been through the Royal Society of Chemistry peer review process and has been accepted for publication.

Accepted Manuscripts are published online shortly after acceptance, before technical editing, formatting and proof reading. Using this free service, authors can make their results available to the community, in citable form, before we publish the edited article. We will replace this Accepted Manuscript with the edited and formatted Advance Article as soon as it is available.

You can find more information about Accepted Manuscripts in the [Information for Authors](#).

Please note that technical editing may introduce minor changes to the text and/or graphics, which may alter content. The journal's standard [Terms & Conditions](#) and the [Ethical guidelines](#) still apply. In no event shall the Royal Society of Chemistry be held responsible for any errors or omissions in this Accepted Manuscript or any consequences arising from the use of any information it contains.

ARTICLE

Tunable Single-Column Deterministic Lateral Displacement Device by Adjustable Crossflow

Miftahul Jannat Rasna^a and James C. Sturm^{*a}Received 00th January 20xx,
Accepted 00th January 20xx

DOI: 10.1039/x0xx00000x

Conventional deterministic lateral displacement (DLD) devices are popular for continuous size-based separation of micro-particles at a high resolution through a tilted array of periodically placed micro-posts. However, the conventional DLD devices lack tunability of the critical size of particle sorting (D_c). In a conventional DLD device, the D_c is fixed by the device geometry. Further, many rows and columns of micro-posts are required in the device array to provide adequate spatial separation between large and small particles after lateral bumping of large particles, which leads to large device area and potentially small throughput/area. In this work, we present a novel tunable single-column DLD device where tunability was demonstrated by adjusting crossflow applied perpendicularly to the main flow direction. Our device consists of only 8 bumping obstacles with a device area of $0.83 \text{ mm} \times 0.24 \text{ mm} = 0.2 \text{ mm}^2$ (without inlet/outlet ports). The ability to tune the critical size D_c from below $5 \mu\text{m}$ to above $10 \mu\text{m}$ in a single structure is demonstrated with a separation efficiency of $\sim 99.9\%$ and the throughput/area is $45 \mu\text{L}/\text{min}$ per mm^2 . Further, at very high flow rates ($\text{Re} > 10$), the resolution degrades due to a three-dimensional fluid flow pattern.

1. Introduction

Particle sorting plays a crucial role in various applications¹, such as – chemical² and biological³ processing, clinical diagnostics^{4,5}, environmental analysis⁶, quality control and regulation enforcement in manufacturing cosmetic products⁷. Deterministic lateral displacement (DLD) is a well-known size-based particle sorting technology for its simple operation, robustness, deterministic physics, and high resolution⁸, first reported by Huang et al. in 2004⁹. DLD technique has shown the ability to separate particles in a wide range of sizes spreading from nanometers¹⁰ to micrometers¹¹. In medical applications, it has also been vastly used to separate biological cells, such as blood cells^{12–15}, circulating tumor cells (CTCs)^{16–21}, DNA^{9,22} and exosomes¹⁰. In the DLD method, particle separation happens due to the flow bifurcation^{9,12} around a set of obstacles (“posts”). Migration of particles follows either the average fluid flow direction or the axis direction of the posts, determined by the “critical size (D_c)” of the device. The particles larger than the critical size “bump” at the posts and follow the micro-array inclination (lateral displacement), whereas smaller particles follow

the macroscale fluid flow direction (zigzag mode). The critical diameter of particle sorting (D_c) is determined by the array geometry, specifically the gap size between two posts and the tilt angle (ϵ)²³ of the micro-array. Hence the critical size cannot be changed.

Further, to increase throughput of conventional DLD devices the number of columns in the DLD array is increased, but at the same time, the number of rows also needs to be increased since each column requires $1/\epsilon$ rows. Hence, the area of a DLD device increases as the square of the throughput, thus decreasing the throughput per area. To increase throughput per area, Liang et al. (2020) introduced a “single-column” DLD device²⁴ where the array of posts is replaced by a single vertical channel with a series of protrusions on one side. A crossflow right after protrusion, set by a series of carefully designed fluidic resistors, sets the critical size, above which large particles were harvested at the end of the vertical channel.

Both the conventional and single-column DLD devices have a critical size for particle harvesting which is set by the fabrication. There have been several attempts to make the critical diameter (D_c) of conventional DLD devices tunable. One of the very early demonstrations of tunability in DLD device was achieved by stretching a PDMS device²⁵. However, its elastomeric flexibility makes a PDMS device suffer in high-pressure applications²⁶. In

^a Department of Electrical Engineering, Princeton University, Princeton, New Jersey, 08544, USA.

^b Address here.

^c Address here.

† Footnotes relating to the title and/or authors should appear here.

Supplementary Information available: [details of any supplementary information available should be included here]. See DOI: 10.1039/x0xx00000x



several studies, dielectrophoresis (DEP) has been coupled with DLD to achieve wide ranges of critical size tuning^{27–30}. However, complex theoretical analysis, complicated fabrication and implementation, high voltage, heating, etc. make this hybrid technique difficult to use in practice. Numerical and experimental studies used non-Newtonian viscoelastic fluids as buffer solution for tuning the D_c ^{31,32}. In one study, acoustic vibrations were passed to PDMS micropillars to switch the trajectory of 2 and 7 μm particles³³. In moderate Reynolds number regime, Dincao et al. (2018) observed streamline evolution and micro vortices in the wake of micro-posts, which shifted the particles trajectory. They were able to switch 10 and 20 μm particles from zigzag mode to displacement mode by increasing Reynolds number by a factor of 6 and 7, respectively³⁴. Tottori and Nisisako demonstrated tuning of D_c by exploiting temperature-controlled swelling and shrinking of hydrogel pillars. However, the characterization of hydrogel pillars and the temperature control need to be very precise to achieve error-free tuning of D_c ³⁵.

In this paper, we demonstrate the first ability to tune the critical diameter D_c of a single-column Deterministic Lateral Displacement device. Particles with diameter below D_c remain in a vertical streamtube of fluid as it moves down through a device, and particles with diameter above D_c are “bumped” by an asymmetric obstacle into an adjacent streamtube so that they leave the initial streamtube of fluid. Tunability is achieved by applying an externally adjustable crossflow set by syringe pumps, applied individually to each row of bumping obstacles. **Fig. 1** presents a schematic diagram of a single-column DLD device with four bumping obstacles tuned by different crossflows (left side I_2 =right side I_3) while keeping the vertical sample flow I_1 fixed. When $I_2=I_3$, the right cross-channels withdraw the same volume of fluid introduced in the left cross-channels. Hence, both the fluid segmentation and thus the critical size D_c are identical at each bump. Here, D_c is double the width of the first streamtube adjacent to the bumping obstacle at the protruding bumping site and it can be tuned by changing the crossflow rate. When crossflow rate ($I_2=I_3$) is increased for a certain sample flow rate (I_1), D_c also increases, because a larger volume of fluid is drawn out from the central channel through the right-sided cross channels. At the same time, a larger volume of fresh buffer is introduced into the central channel through the left cross channels to keep the amount of fluid same there and to replace sample fluid with fresh buffer. In a conventional DLD with triangular posts, the critical diameter, D_c can be determined by the well-known experimental fit as follows^{36–38}

$$D_c = G \left(\frac{1}{N} \right)^{0.48} = G \epsilon^{0.48}$$

where, G is the gap size between adjacent posts and N is the row periodicity ($\frac{1}{\epsilon}$). G and N are both fixed by the device geometry. In our tunable single column DLD device, the ratio of the flow rates ($\frac{\text{crossflow rate}}{\text{sample flow rate}}$) is the equivalent of ϵ and hence $\frac{1}{N}$. Thus, the expected critical size is

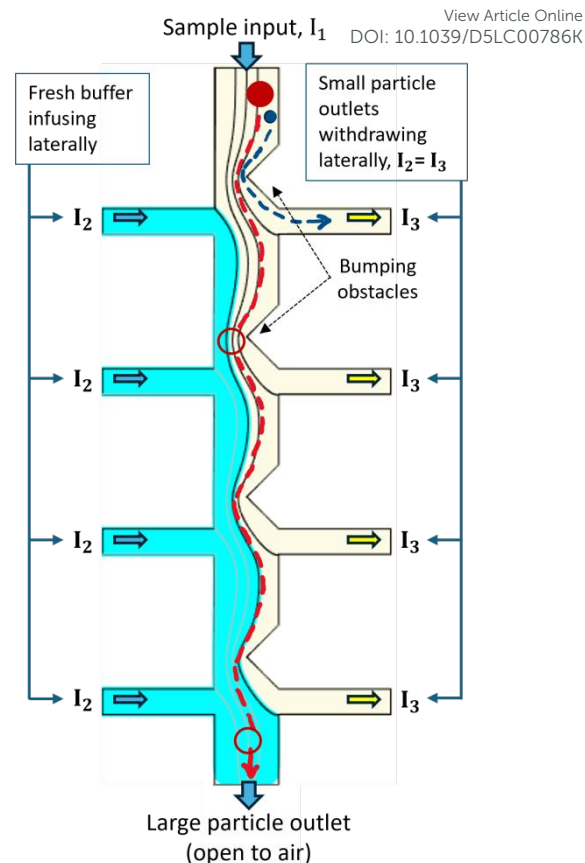


Fig. 1 Schematic diagram of a tunable single-column DLD device with four bumping obstacles. Sample with particles enters vertically with a flowrate of I_1 . The cross channels on the left side introduce fresh buffer each at a flowrate of I_2 , and the cross channels on the right side withdraw fluid from the main channel at a flowrate of I_3 , where $I_2 = I_3$. The streamlines at the bumping sites which bifurcate the flow between the main channel and the right-sided cross channels are called segmentation streamlines. At the bumping site, a particle (blue) smaller than D_c will not bump and will go to the small particle outlet. Whereas a particle (red) larger than D_c will bump and be pushed towards the next streamline and continue to travel through the main channel.

$$D_c = G \left(\frac{1}{N} \right)^{0.48} = G \epsilon^{0.48} \\ = G \left(\frac{\text{Crossflow rate in each row}}{\text{Sample flow rate}} \right)^{0.48}$$

Since we can control the ratio of flowrates by adjusting crossflow, we are not limited by the device geometry (meaning arrangement of obstacles), and our device is tunable with fewer bumps arranged in a single-column channel, enabling high throughput per area.

In this study, we perform two sets of experiments in the moderate Reynolds number regime ($5 < Re < 30$). The Reynolds number (Re), in a DLD array is defined as³⁹



$$Re = \frac{\rho u L_0}{\eta}$$

where, ρ is the density of water at room temperature, u is the average velocity of the fluid in the gap, L_0 is the characteristic length of the gap (in our case, hydraulic diameter of a rectangular channel), and η is the dynamic viscosity of water. In the first set of experiments, we separate 5, 8.2 and 10 μm particles from each other with $\sim 100\%$ efficiency at a throughput of 45 $\mu\text{L}/\text{min}$ per mm^2 . In the second set of experiments, we explore the effect of increasing Re on the tuning performance of our single-column DLD device and propose a mechanism for its degradation.

2. Materials and Methods

2.1 Device design

The design of a single-column DLD device follows the design of conventional multi-column DLD arrays: **(i)** In a conventional DLD array, from one row to the next, the carrier fluid in each gap divides in the next gap, with most staying in the current column and some fraction going to the next column, because of the “tilt” of the array axis vs. the average fluid flow direction⁹. This fraction is set by the number of rows before fluid at one position in a gap is in the same position at the next adjacent gap – the inverse of the so called “tilt

angle”, ϵ . **(ii)** In a “single column” DLD device, the “effective tilt” (bifurcation of the vertical flow) is set by the amount of fluid injected into the main column vertical from a side channel. Similarly, the same amount of fluid also flows out the opposite side. This is described in detail in the first (non-tunable) single column DLD²⁴ published by Liang et al. (2020). In that paper, this fraction was set by fluidic resistors (determined by the device fabrication). In this paper, the dimensions of cross channels and the protrusion length of bumping obstacles are based on prior work on single-column DLD²⁴. However, the hydraulic resistance of cross channels does not matter since the horizontal flow component is determined by flowrate-controlled syringe pumps, making the critical size tunable. The channel height is chosen to have a moderate aspect ratio (height/width on the order of 1) for ease of microfabrication.

Our tunable single-column DLD device consists of 8 bumping obstacles. The width of the central bumping column is 38 μm , and the narrowed gap region at each of the bumping sites is 18 μm wide. The protrusion width of each triangular bumping obstacle (parameter “ b ” in Fig. 2) is 20 μm . The width of the cross channels on both sides on the central column is 16 μm . The device is 826 μm long, 238 μm wide, and 28 μm high (not including the inlet/outlet ports).

It is fundamental to the operation of a DLD array that the critical diameter depends on the shape and arrangement of the posts (bumping obstacles)^{36,37}. The triangular shape of posts instead of circular posts allow larger gaps for the same critical size, hence reducing clogging and enabling higher throughput for a given pressure gradient⁴⁰. Thus, for our single-column devices, we have used triangular posts.

2.2 Device fabrication and experimental setup

We fabricated our device on 500 μm thick silicon wafer using standard microfabrication technique. A SAMCO RIE800iPB reactivation etcher was used to etch the channels to a depth of 28 μm and the angle between the vertical wall and the channel floor was approximately 90°. The inlets and outlets were 300 μm through-holes obtained by etching through the silicon wafer from the backside. After performing standard chemical cleaning of silicon wafer, we sealed the device with a polyolefin sealing tape (9795RR, 3M, USA). The device was mounted to an acrylic manifold with stainless steel microtubes.

An inverted microscope was used for imaging the particle movement. Images and videos were captured with 10X Nikon Plan fluor objective (0.30 NA and 16 mm WD) and ORCA-Flash4.0 digital camera C11440 from Hamamatsu Photonics. We have used three flowrate-controlled syringe pumps (Chemyx Fusion 200) which can be used in either ‘infusion’ or ‘withdraw’ mode. At the sample inlet, we used one syringe pump in ‘infusion’ mode. For the eight fresh buffer inlets, we have mounted a 10-syringe expansion rack on a Fusion 200 syringe pump and operated it in ‘infusion’ mode. At the small particle outlets, we used another syringe pump with a 10-syringe expansion rack in the ‘withdraw’ mode.

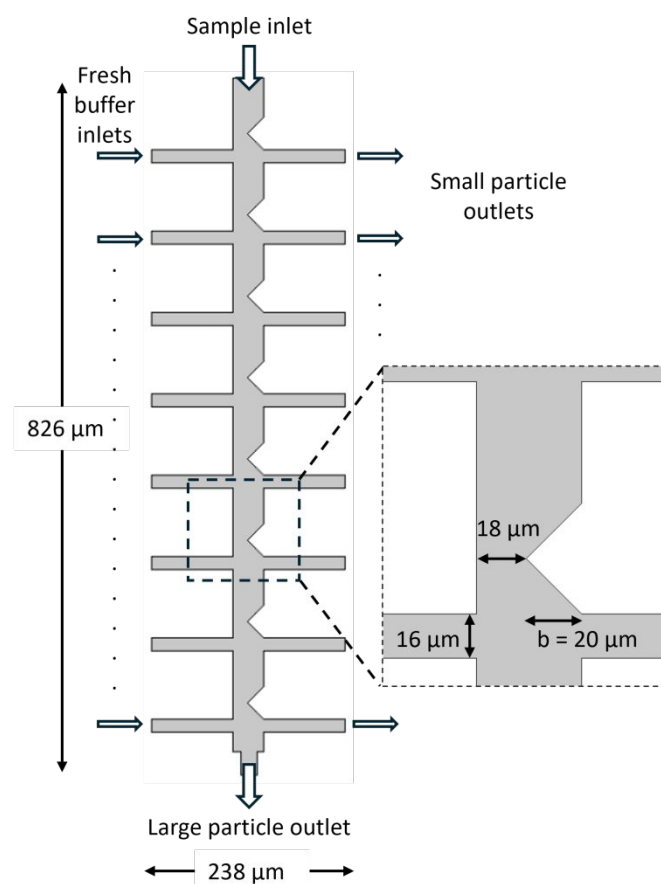


Fig. 2 The 8-bump design of the tunable single-column DLD device used in our experiments.



2.3 Preparation of experimental samples

Device functionality for various flowrates was confirmed by observing the trajectories of three sizes of fluorescent particles, which are Thermo Scientific™ Fluoro-Max Dye Green Aqueous Fluorescent Polymer Microsphere, 5 and 10 μm (10 mL), and, DiagPoly™ Green Fluorescent Polystyrene Particles, 8.2 μm (1 mL). We have diluted these particles in 0.1% Tween 20 surfactant in DI water to achieve a concentration of 700 to 1000 particles per microliter of sample.

3 Results and Discussion

3.1 Experiments

3.1.1 Tuning of the Critical Size

In our first experiment, we ran samples containing 5, 8.2 and 10 μm particles through the sample inlet of our device at a fixed sample (vertical) flow rate of 9 $\mu\text{L}/\text{min}$ in each channel which gives a channel Reynolds number of 7.4 at the narrowed bumping region. When we varied the crossflow rates from 0 to 4.5 $\mu\text{L}/\text{min}$, all the 5 μm particles stop bumping at the crossflow rate of 1.5 $\mu\text{L}/\text{min}$ and go to small particle outlets. However, the 8.2 and 10 μm particles still bump at the obstacles and reach the large particle outlet (Fig. 3a). Since, there are 8 rows of cross channels in our device, a crossflow rate of 1.5 $\mu\text{L}/\text{min}$ at each cross channel fully replace the sample fluid by the 6th row ($6 \times 1.5 \mu\text{L}/\text{min} = 9 \mu\text{L}/\text{min}$). Hence, at 1.5 $\mu\text{L}/\text{min}$, we have large particles in the fresh buffer at the large particle outlet. As we increase the crossflow rate to 2.5 $\mu\text{L}/\text{min}$, all the 8.2 μm particles go to small particle outlet along with 5 μm particles. However, the 10 μm particles still end up in the large particle outlet (Fig. 3b).

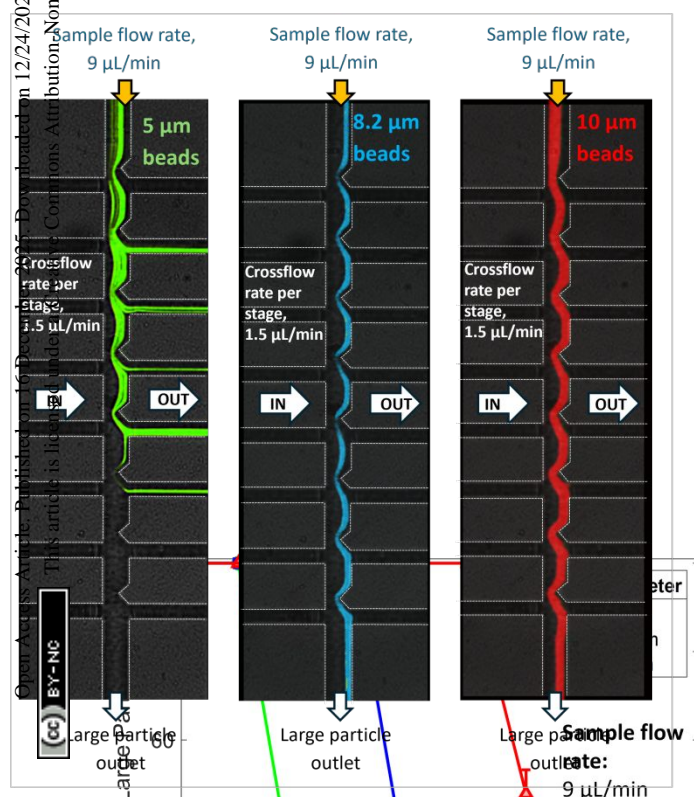


Fig. 3a

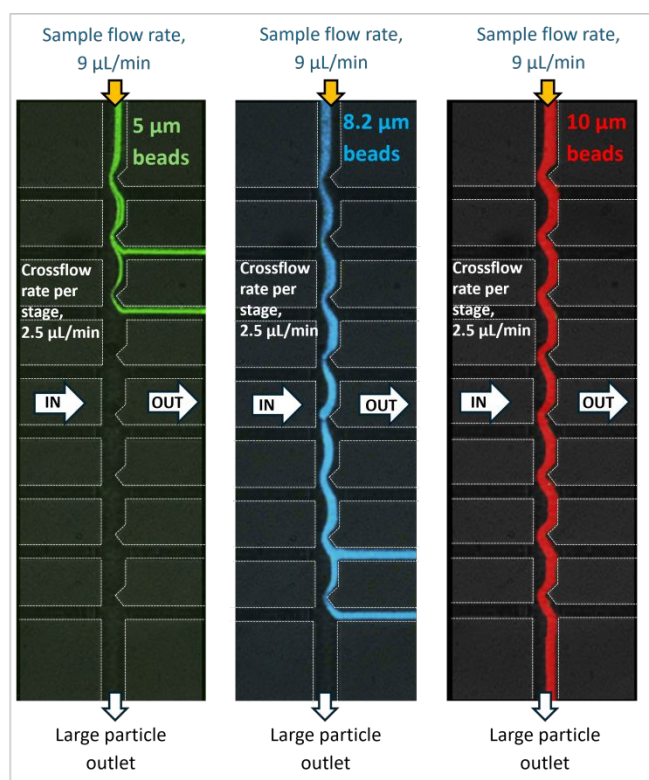


Fig. 3b

Fig. 3 At sample flow rate of 9 $\mu\text{L}/\text{min}$, fluorescent images showing separation between **a)** 5 μm and 8.2 μm particles at crossflow rate of 1.5 $\mu\text{L}/\text{min}$; **b)** 8.2 μm and 10 μm particles at crossflow rate of 2.5 $\mu\text{L}/\text{min}$. The channel Reynolds number is 7.4. As we increase the crossflow, larger volume of fluid leaves the central column through the small particle outlets on the right-side. The streamtubes entering the small particle outlets get wider at higher cross flow. The critical diameter, D_c also increases. As a result, smaller particles stop bumping and end up in small particle outlets. The higher we increase the crossflow, the sooner the smaller particles go to small particle outlet. The dotted structures show the approximate position of the channels.

Fig. 4 Experimental results showing the fraction of 5, 8.2 and 10 μm particles in the large particle outlet at various $\frac{\text{crossflow rate}}{\text{sample flow rate}}$ for sample flow rate of 9 $\mu\text{L}/\text{min}$. The vertical bars indicate variation in the percentage of particle concentration in the large particle outlet during the transition in the traveling modes of particles.

Finally, when we increase the crossflow rate to 3.5 $\mu\text{L}/\text{min}$, ~99% of the 10 μm particles stop bumping and end up in small particle outlets as well. **Fig. 4** represents the recovery curves of 5, 8.2 and 10 μm particles at sample flow rate of 9 $\mu\text{L}/\text{min}$. The x-axis is presented as the ratio of crossflow rate to sample flow rate.

In this work, the channel area (without inlet/outlet ports) is: $0.83 \text{ mm} \times 0.24 \text{ mm} = 0.2 \text{ mm}^2$. Hence, a sample flow rate of $9 \mu\text{L}/\text{min}$ gives a throughput per area of $45 \mu\text{L}/\text{min per mm}^2$.

3.1.2. High Flow Rate Effects

To understand the separation performance of our device at higher flowrates, next we performed a series of experiments with $5 \mu\text{m}$ particles at various sample flow rates and hence various moderate Reynolds numbers ($5 < \text{Re} < 30$), and we vary the crossflow rates in each case to see bumping behaviour of $5 \mu\text{m}$ particles (Fig. 5). As we increased the sample flow rates, the sharpness of the recovery curves of $5 \mu\text{m}$ particles in the large particle outlet was reduced. Particles showed a tendency to begin bumping earlier (lower crossflow) and stop bumping at a larger crossflow rate when sample flow increased. When sample flow rate is $9 \mu\text{L}/\text{min}$, all the $5 \mu\text{m}$

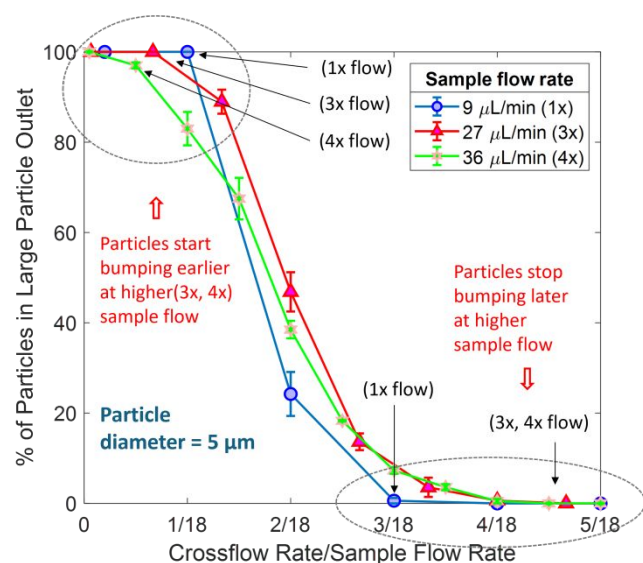


Fig. 5 Experimental results showing the fraction of $5 \mu\text{m}$ particles in the large particle output for various sample and crossflow rates. The X-axis is shown as the ratio of crossflow to sample flow rates. Here, the channel Reynolds numbers are 7.4, 22 and 29.4 in the ascending order of sample flow rates. The vertical bars indicate variation in the percentage of particle concentration in the large particle outlet during the transition in the traveling modes of particles.

particles stop bumping at crossflow rate of $1.5 \mu\text{L}/\text{min}$. Here, $\frac{\text{crossflow rate}}{\text{sample flow rate}} = \frac{1}{6}$. But when we triple the sample flow rate ($27 \mu\text{L}/\text{min}$), the $5 \mu\text{m}$ particles do not fully stop bumping at tripled crossflow rate of $4.5 \mu\text{L}/\text{min}$. Rather they show a 'mixed mode', where some particles still go to the large particle outlet, and the rest of the $5 \mu\text{m}$ particles go to small particle outlets. To stop all the $5 \mu\text{m}$ particles from going to the large particle outlet, we need to increase the $\frac{\text{crossflow rate}}{\text{sample flow rate}}$. As the sample flowrate increases, the sharpness of the recovery curve reduces.

3.2 Three-dimensional analysis of streamlines in COMSOL

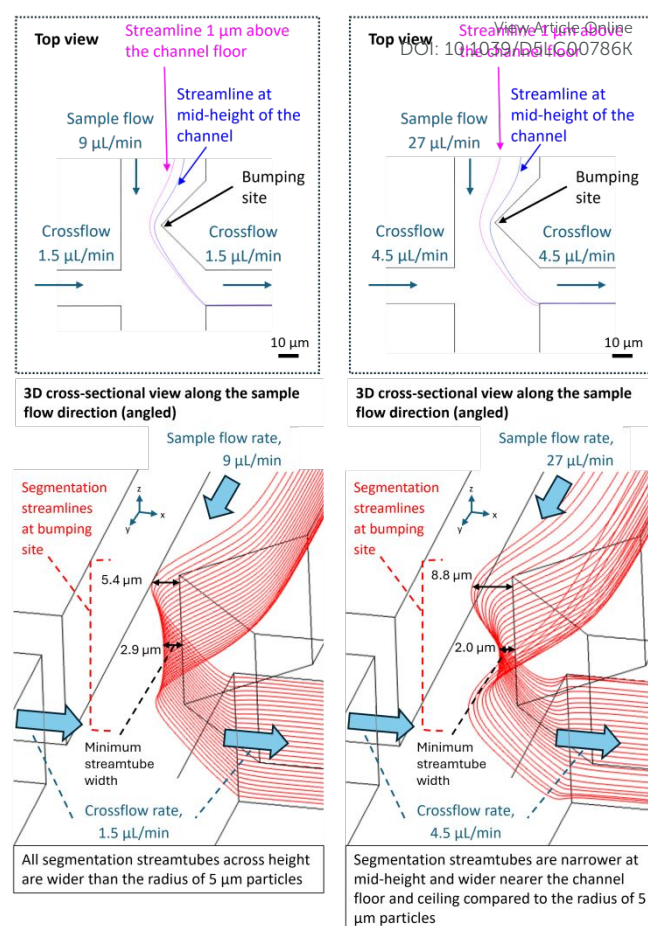


Fig. 6a ($\text{Re} = 7.4$)

Fig. 6b ($\text{Re} = 22$)

Fig. 6 COMSOL 3D simulations of segmentation streamlines at the bumping site for two Reynolds numbers in the moderate regime. The top panels (dashed outlined) show the device top view, while the bottom panels present cross-sectional views along the flow direction at an angled perspective. Coordinate axes: x = crossflow, y = sample flow, z = channel height ($28 \mu\text{m}$). The $\frac{\text{crossflow rate}}{\text{sample flow rate}} = \frac{1}{6}$ in both cases. (a) Sample flow = $9 \mu\text{L}/\text{min}$ ($\text{Re} = 7.4$), crossflow = $1.5 \mu\text{L}/\text{min}$. (b) Sample flow = $27 \mu\text{L}/\text{min}$ ($\text{Re} = 22$), crossflow = $4.5 \mu\text{L}/\text{min}$. In the top views, Magenta streamlines are taken $1 \mu\text{m}$ above the channel floor; blue streamlines are at mid-height. With higher crossflow, the segmentation streamtube width shows greater variation between mid-height and near the floor/ceiling.

To understand this compromised resolution of recovery curves at higher sample flow rates, we performed 3-dimensional streamline analysis of our tunable single-column DLD device. We ran a grid-independency test for COMSOL with various default sizes of mesh, and the results here are obtained after we see no variation with increasing mesh fineness. We make the simplifying assumption that unless bumping against a wall, particles follow the streamlines. This is justified by the fact that for $\text{Re} = 22$ (or lower), fluid flow is still laminar⁴¹.

The critical diameter of particle sorting (D_c) is twice the width of the streamtube at the bumping site that leaves the main channel and

enters the small particle outlet. The streamline which divides the flow at the junction of main channel and the small particle outlet is called the segmentation streamline. 3D simulations allow us visualizing the segmentation streamlines across channel height at the bumping site⁴². In **Fig. 6**, we show the segmentation streamlines at the bumping site across height for sample flowrates of 9 $\mu\text{L}/\text{min}$ ($\text{Re} = 7.4$) and 27 $\mu\text{L}/\text{min}$ ($\text{Re} = 22$) while keeping the $\frac{\text{crossflow rate}}{\text{sample flow rate}}$ constant. The width of the corresponding streamtubes varies from the center of the channel to the channel floor and the channel ceiling at the bumping site. i.e. across the height of the device. This means that the maximum “critical size” of particles that go to the “small particle outlet” is larger near the top and bottom of the channel than in the middle.

However, this variation is more pronounced at the higher Reynolds number. At sample flow of 9 $\mu\text{L}/\text{min}$ ($\text{Re} = 7.4$) and crossflow of 1.5 $\mu\text{L}/\text{min}$, all the segmentation streamtubes are wider than 2.5 μm (**Fig. 6a**). Hence the predicted bumping radius (r_c) at all heights within the device is larger than the radius of 5 μm particles. As a result, none of the 5 μm particles bump at the obstacle anymore and they simply go to waste. However, at sample flow of 27 $\mu\text{L}/\text{min}$ ($\text{Re} = 22$) and crossflow of 4.5 $\mu\text{L}/\text{min}$ ($\frac{\text{crossflow rate}}{\text{sample flow rate}}$ is same as previous case), the width of the segmentation streamtubes at the bumping site is narrower than 2.5 μm at mid-height of the device (**Fig. 6b**), wider

to the small-particle outlet. the 5 μm particles travel in a “mixed” bumping mode at larger sample flowrates, as observed in **Fig. 5**.

In **Fig. 7**, we plot the width of segmentation streamtubes (predicted bumping radius) across height for various Reynolds numbers ranging from 0.001 to 29, with $\frac{\text{crossflow rate}}{\text{sample flow rate}} = \frac{1}{6}$. We can see that, the width of streamtubes from mid-height to floor (or ceiling) of the channel is minimum and the plots of streamtubes at different depths are similar, with the streamtubes collapsing on top of each other when $\text{Re} \leq 1$. Whereas, when $\text{Re} > 1$, the variation in the width of the segmentation streamtubes increases as we go higher Reynolds numbers. For example, at sample flow of 9 $\mu\text{L}/\text{min}$ ($\text{Re} = 7.4$) and $\frac{\text{crossflow rate}}{\text{sample flow rate}} = \frac{1}{6}$, we demonstrated the separation of 5 μm particles from 8.2 μm particles (**Fig. 4**). However, at sample flow 1.5 $\mu\text{L}/\text{min}$ ($\text{Re} = 1.2$) and same cross- to sample flow rate ratio, 6.5 μm particle could potentially be separated from 8 particles (according to the predicted bumping radii in **Fig. 7**). Separation resolution could be improved by two-fold, but throughput would be compromised by six-fold.

The enhanced variation in the width of segmentation streamtubes (at high Re) across height of the channel depends on the velocity fields of fluid molecules at the bumping site and near the small particle outlet, because velocity field directions are tangent to streamlines. At high flowrates, nonlinear effects³⁹ (inertial) cause flow patterns to differ from their low velocity conditions. That is exhibited in **Fig. 6** (6a. low velocity vs. 6b. high velocity). Reducing channel height while keeping the channel width constant would lead to smaller hydraulic diameter which is also the characteristic length in our calculation of Reynolds number. The ratio of volume to surface forces would be reduced to lower the inertial effects³⁹.

3.3 Discussion

This work addresses two major challenges in deterministic lateral displacement (DLD): the tunability of the critical diameter (D_c) combined with a high throughput per area.

Table 1 provides a quantitative comparison of our device against other size-based particle separation methods operating in a similar dynamic size range (sizes of red and white blood cells). Here, throughput represents the total sample flow rate. Particle size is presented in diameters. Separation efficiency has been defined as the yield or the percentage of large particles that are successfully collected in the intended outlet (large particle outlet). The device area and throughput per area are determined without including the inlet/outlet ports for our device, single-column DLD with fixed D_c ²⁴ and HDF device⁴³. Compared to a previous high-throughput but non-tunable DLD device⁴⁴, our design achieves tunable D_c with more than a 2.5-fold increase in throughput per area and over a 6-fold improvement in size resolution, all with higher separation efficiency. Although tunable DLD devices based on hydrogel pillars³⁵ have shown D_c adjustability, to date they exhibit $\sim 2\times$ lower size resolution and ~ 2.5 orders of magnitude lower throughput per area. Our device

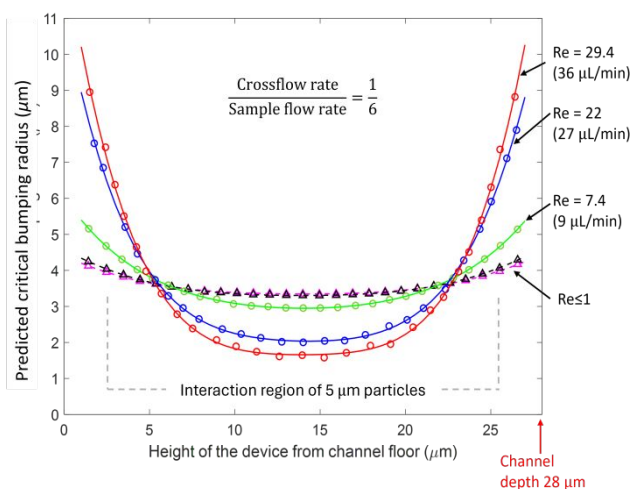


Fig. 7 COMSOL simulations of the variance of the width of segmentation streamtubes across channel height for different sample flowrates and hence different Reynolds numbers while we keep $\frac{\text{crossflow rate}}{\text{sample flow rate}}$ fixed at $\frac{1}{6}$. The interaction region of 5 μm particles are showed as grey horizontal dotted lines based on the corresponding radius of 2.5 μm .

nearer the top and bottom of the channel (device ceiling and floor). This explains why at high flow rates, some of the 5- μm particles (the ones near the middle of the channel) “bump” and go the “large-particle” outlet, whereas those near the top and bottom of the channel, where the bumping radii are large, do not “bump” and go



Table 1 Performance comparison between different microfluidic cell sorters (particle sizes are diameters)

View Article Online
DOI: 10.1039/D5LC00786K

Technology	Fundamental principle	Small particle	Large particle	Ratio of particle sizes separated (small/large)	Separation efficiency	Throughput (μL/min)	Device area (mm ²)	Throughput/area (μL/min/mm ²)	Tunability of D _c
Clot formation-inhibited DLD ⁴⁴	• array with circular posts operating at Re ~ 10	RBC	PC3 (17 μm)	0.29	86%	1470	85	17.3	No
Tunable conventional DLD ³⁵	• hydrogel micropillars • swelling/shrinking of pillar width based on device temperature to adjust the gap between pillars	Beads (2.1 μm)	Beads (7.3 μm)	0.28	99.99%	8.3	60	0.14 (device temperature is 24 ^o C)	Yes. At 35°C, 7.3 μm particles shift from displacement to zigzag mode
Hydrodynamic filtration ⁴³	• rectangular microchannel passively splitting flow into side channels • flow ratios set by channel geometry	RBC (<3 μm)	Leukocytes (>8 μm)	0.38	99.99% (2 rounds of filtration)	20	0.6	33	No
Single-column DLD with fixed critical size ²⁴	• rectangular channel consisting of with bumps on one side • D _c determined by a crossflow after each bump, fixed by the fluidic resistors of side channels	Beads (4.8 μm)	Beads (9.9 μm)	0.48	99.99%	30	0.56	53.5	No
This work	• single-column tunable DLD consisting of side channels and adjustable crossflow after each bump • critical size is set by the adjustable crossflow	Case 1: beads (5 μm)	Case 1: beads (8.2 μm)	0.61	99.99%	9	0.2	45	Yes
		Case 2: beads (8.2 μm)	Case 2: beads (10 μm)	0.82					

shares some functional features with both hydrodynamic filtration (HDF) devices⁴³ and single-column non-tunable DLD device²⁴, where particles follow streamtubes into side channels when their radius is smaller than the streamtube width near a bump or wall. However, unlike those approaches, D_c in our device is not fixed by the channel geometry, and our device provides tunability to crossflow control and achieves more than 2.5x higher size resolution. Further, the “large particle outlet” of our device is not contaminated by some “small particles” which inevitably remain in the central channel at each stage, as in HDF.

We have discussed in the introduction that, the $\frac{\text{crossflow rate}}{\text{sample flow rate}}$ in our tunable single-column DLD device is the equivalent of the tilt angle (row shift fraction), ϵ , which is $(\frac{1}{N})$, where N is the row periodicity in conventional DLD devices. In Fig. 8, we plotted data comparing the critical size (D_c) vs. row shift fraction (for the same gap size, G) for a conventional DLD and the effective row shift fraction for new device in this work. While qualitative agreement is good, there is about $\leq 15\%$ deviation between our experimental data for tunable single-column DLD device and the empirical fit for conventional DLDs. The discrepancy may arise from the Reynolds number effects. Our data were obtained at Re = 7.4, whereas the empirical fit^{23,37,38} for conventional DLDs with triangular posts was obtained for Re < 1.

In this work, we have experimentally demonstrated tuning of the critical size by greater than a factor of 2. The width of the narrow

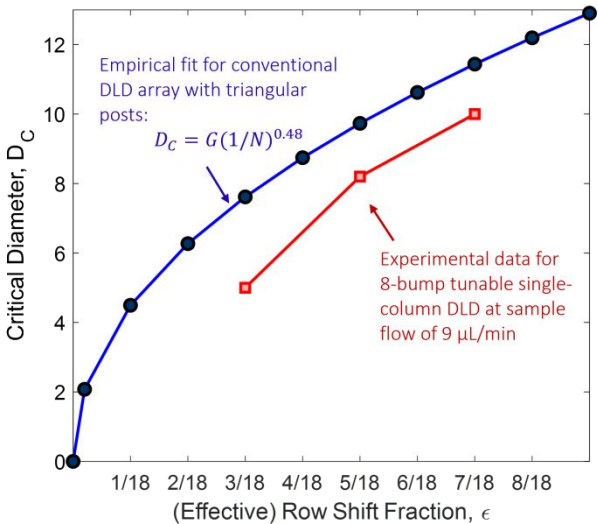


Fig. 8 Comparison of the plots of “Critical diameter, D_c vs. the (effective) row shift fraction, ϵ for conventional DLD devices^{36,37} (empirical fit) and tunable single-column DLD device (experimental data presented in Fig. 4). The effective row shift fraction in the new device is $\frac{\text{crossflow rate in each row}}{\text{sample flow rate}}$, whereas for conventional DLDs, the row shift fraction, $\epsilon = \frac{1}{N}$. Here, N is the row periodicity in conventional DLDs.

“gap” in our device which gives rise to the “bumping” of large particles to adjacent streamtubes (which is the physical mechanism of the particle separation in DLD) is 18 μm . Theoretically, the maximum achievable critical size can be just below this gap size³⁶, though we limited experiments to 10 μm (upper size limit) to avoid clogging. The lower bound of critical size tuning depends on smaller crossflow rates. However, in our single-column device, using smaller crossflow rates (for the same vertical flow) require more rows (larger N) to separate large and small particles (as in convention DLD arrays), and hence more syringe pumps. Thus, right now we are limiting our interest to devices with $N < 10$. A single-column DLD device with 8 rows of cross channels, an 18 μm gap and a sample flow of 9 $\mu\text{L}/\text{min}$ would require at least 1.1 $\mu\text{L}/\text{min}$ per cross-channel to fully replace the sample with buffer at the large-particle outlet. Numerical simulation (not shown here) shows that this would limit the minimum achievable critical size to 4.8 μm .

Apart from limiting the maximum tunable size during experiments to minimize device clogging, the sample was prepared with anti-clogging additives (section 2.3), and was filtered through 20 μm cell strainers⁴⁵. Further, integrated pre-filters were added to the inlet channel design of our device to remove cell aggregates in sample⁴⁶. In a conventional DLD array⁴⁷ with a width of 40 mm, a throughput of 70 mL/h has been reported, which corresponds to approximately 67 $\mu\text{L}/\text{h}$ for a single-column device with a 38 μm width. In contrast, our single-column DLD device, with an inlet width of only 38 μm , achieved a sample throughput of 2 mL/h containing roughly 1000 particles/ μL , operating continuously for 7 hours without clogging. Future work is aimed at extending this concept to multiple integrated vertical channels in parallel and ultimately to a tunable deterministic lateral displacement device.

Conclusion

In summary, we have demonstrated a novel tunable single-column deterministic lateral displacement device where we performed particle separation in the 5–10 μm range with ~99.9 % efficiency by applying an adjustable crossflow. It achieves very high throughput/area due to small device dimensions. The separation performance degrades with increasing Reynolds number (increasing sample throughput) due to an increased variation in critical size across the depth of the device at the bumping site.

Author contributions

Miftahul Jannat Rasna: Conceptualization (equal), Data curation, Formal analysis, Investigation, Methodology, Software, Validation (equal), Visualization (equal), Writing – original draft Writing.

James C. Sturm: Conceptualization (equal), Funding acquisition, Project administration, Resources, Supervision, Validation (equal), Visualization (equal), Writing – review & editing.

Conflicts of interest

There are no conflicts to declare.

View Article Online
DOI: 10.1039/D5LC00786K

Data availability

Significant images, data and modelling results have been presented in the manuscript. The importance of protruding obstacles in our device to ‘bump’ large particles is described in Supplementary Information (SI). References 24 and 43 in this article’s reference list are cited in the Supplementary Information (SI). More image data and COMSOL models can be made available to readers. Please contact the authors if required.

Acknowledgements

The authors gratefully acknowledge Howard A. Stone and Nan Hu of the Department of Mechanical and Aerospace Engineering at Princeton University for helpful discussion on fluid mechanics, and the staff of the Princeton Micro/Nanofabrication and Packaging labs.

Notes and references

1. Alix-Panabières, C. & Pantel, K. Challenges in circulating tumour cell research. *Nat. Rev. Cancer* **14**, 623–631 (2014).
2. Reyes, D. R., Iossifidis, D., Auroux, P.-A. & Manz, A. Micro total analysis systems. 1. Introduction, theory, and technology. *Anal. Chem.* **74**, 2623–2636 (2002).
3. Toner, M. & Irimia, D. Blood-on-a-chip. *Annu. Rev. Biomed. Eng.* **7**, 77–103 (2005).
4. Watanabe, M. *et al.* Isolation and molecular analysis of circulating tumor cells from lung cancer patients using a microfluidic chip type cell sorter. *Cancer Sci.* **109**, 2539–2548 (2018).
5. Farahinia, A., Zhang, W. & Badea, I. Recent Developments in Inertial and Centrifugal Microfluidic Systems along with the Involved Forces for Cancer Cell Separation: A Review. *Sensors* **23**, 5300 (2023).
6. Tóth, E. L., Holczer, E., Földes, P., Iván, K. & Fürjes, P. Microfluidic Particle Sorting System for Environmental Pollution Monitoring Applications. *Procedia Eng.* **168**, 1462–1465 (2016).
7. Sogne, V., Meier, F., Klein, T. & Contado, C. Investigation of zinc oxide particles in cosmetic products by means of centrifugal and asymmetrical flow field-flow fractionation. *J. Chromatogr. A* **1515**, 196–208 (2017).



8. Salafi, T., Zhang, Y. & Zhang, Y. A Review on Deterministic Lateral Displacement for Particle Separation and Detection. *Nano-Micro Lett.* **11**, 77 (2019).
9. Continuous Particle Separation Through Deterministic Lateral Displacement | Science. <https://www.science.org/doi/full/10.1126/science.1094567>.
10. Wunsch, B. H. *et al.* Nanoscale lateral displacement arrays for the separation of exosomes and colloids down to 20 nm. *Nat. Nanotechnol.* **11**, 936–940 (2016).
11. Au, S. H. *et al.* Microfluidic Isolation of Circulating Tumor Cell Clusters by Size and Asymmetry. *Sci. Rep.* **7**, 2433 (2017).
12. Deterministic hydrodynamics: Taking blood apart | PNAS. <https://www.pnas.org/doi/abs/10.1073/pnas.0605967103>.
13. Automated leukocyte processing by microfluidic deterministic lateral displacement - Civin - 2016 - Cytometry Part A - Wiley Online Library. <https://onlinelibrary.wiley.com/doi/full/10.1002/cyto.a.23019>.
14. Tottori, N. & Nisisako, T. Degas-Driven Deterministic Lateral Displacement in Poly(dimethylsiloxane) Microfluidic Devices. *Anal. Chem.* **91**, 3093–3100 (2019).
15. Label-Free Biophysical Markers from Whole Blood Microfluidic Immune Profiling Reveal Severe Immune Response Signatures - Zeming - 2021 - Small - Wiley Online Library. <https://onlinelibrary.wiley.com/doi/full/10.1002/sml.202006123>.
16. Deterministic separation of cancer cells from blood at 10 mL/min | AIP Advances | AIP Publishing. <https://pubs.aip.org/aip/adv/article/2/4/042107/21631>.
17. Liu, Z. *et al.* Rapid isolation of cancer cells using microfluidic deterministic lateral displacement structure. *Biomicrofluidics* **7**, 011801 (2013).
18. Aghaamoo, M., Aghilinejad, A., Chen, X. & Xu, J. On the design of deterministic dielectrophoresis for continuous separation of circulating tumor cells from peripheral blood cells. *ELECTROPHORESIS* **40**, 1486–1493 (2019).
19. Bioinspired Engineering of a Multivalent Aptamer-Functionalized Nanointerface to Enhance the Capture and Release of Circulating Tumor Cells - Song - 2019 - Angewandte Chemie International Edition - Wiley Online Library. <https://onlinelibrary.wiley.com/doi/full/10.1002/anie.201809337>. DOI: 10.1039/D5LC00786K
20. Tottori, N. & Nisisako, T. Particle/cell separation using sheath-free deterministic lateral displacement arrays with inertially focused single straight input. *Lab. Chip* **20**, 1999–2008 (2020).
21. Liu, Z. *et al.* Cascaded filter deterministic lateral displacement microchips for isolation and molecular analysis of circulating tumor cells and fusion cells. <https://doi.org/10.1039/D1LC00360G> (2021) doi:10.1039/D1LC00360G.
22. Chen, Y. *et al.* Concentrating Genomic Length DNA in a Microfabricated Array. *Phys. Rev. Lett.* **114**, 198303 (2015).
23. Inglis, D. W., Davis, J. A., Austin, R. H. & Sturm, J. C. Critical particle size for fractionation by deterministic lateral displacement. *Lab. Chip* **6**, 655–658 (2006).
24. Liang, W., Austin, R. H. & Sturm, J. C. Scaling of deterministic lateral displacement devices to a single column of bumping obstacles. *Lab. Chip* **20**, 3461–3467 (2020).
25. Beech, J. P. & Tegenfeldt, J. O. Tuneable separation in elastomeric microfluidics devices. *Lab. Chip* **8**, 657–659 (2008).
26. Rein, C., Toner, M. & Sevenler, D. Rapid prototyping for high-pressure microfluidics. *Sci. Rep.* **13**, 1232 (2023).
27. Chang, S. & Cho, Y.-H. A continuous size-dependent particle separator using a negative dielectrophoretic virtual pillar array. *Lab. Chip* **8**, 1930–1936 (2008).
28. Beech, J. P., Jönsson, P. & Tegenfeldt, J. O. Tipping the balance of deterministic lateral displacement devices using dielectrophoresis. *Lab. Chip* **9**, 2698–2706 (2009).
29. Active Posts in Deterministic Lateral Displacement Devices - Beech - 2019 - Advanced Materials Technologies - Wiley Online Library. <https://advanced.onlinelibrary.wiley.com/doi/full/10.1002/admt.201900339?msocid=29c458c559d1678e0a844c35587966b4>.
30. Calero, V., Garcia-Sanchez, P., Honrado, C., Ramos, A. & Morgan, H. AC electrokinetic biased deterministic lateral displacement for tunable particle separation. *Lab. Chip* **19**, 1386–1396 (2019).
31. D'Avino, G. Non-Newtonian deterministic lateral displacement separator: theory and simulations. *Rheol. Acta* **52**, 221–236 (2013).



32. Li, Y. *et al.* Dynamic control of particle separation in deterministic lateral displacement separator with viscoelastic fluids. *Sci. Rep.* **8**, 3618 (2018).
33. Fukunaga, H., Tottori, N., Sakuma, S., Hayakawa, T. & Yamanishi, Y. Tunable Particle Separation Through Acoustic Deterministic Lateral Displacement Micropillar Arrays: 37th IEEE International Conference on Micro Electro Mechanical Systems, MEMS 2024. *IEEE 37th Int. Conf. Micro Electro Mech. Syst. MEMS 2024* 1142–1145 (2024). doi:10.1109/MEMS58180.2024.10439594.
34. Dincau, B. M., Aghilinejad, A., Hammersley, T., Chen, X. & Kim, J.-H. Deterministic lateral displacement (DLD) in the high Reynolds number regime: high-throughput and dynamic separation characteristics. *Microfluid. Nanofluidics* **22**, 59 (2018).
35. Tottori, N. & Nisisako, T. Tunable deterministic lateral displacement of particles flowing through thermo-responsive hydrogel micropillar arrays. *Sci. Rep.* **13**, 4994 (2023).
36. D'Silva, J. High-Throughput Microfluidic Capture of Rare Cells from Large Volumes of Blood. <https://dataspace.princeton.edu/handle/88435/dsp014b29b8392> (2016).
37. Louthback, K. Microfluidic Devices for High Throughput Cell Sorting and Chemical Treatment.
38. Davis, J. A. Microfluidic separation of blood components through deterministic lateral displacement. (Princeton University, United States -- New Jersey, 2008).
39. Bruus, H. *Theoretical Microfluidics*. (Oxford University Press, 2007).
40. Louthback, K. *et al.* Improved performance of deterministic lateral displacement arrays with triangular posts. *Microfluid. Nanofluidics* **9**, 1143–1149 (2010).
41. Manoorkar, S. & Morris, J. F. Particle motion in pressure-driven suspension flow through a symmetric T-channel. *Int. J. Multiph. Flow* **134**, 103447 (2021).
42. Biological Cell Preparation and On-Chip Particle Sorting Systems at High Flow Rate - ProQuest. <https://www.proquest.com/docview/2679594148?fromopenview=true&pq-origsite=gscholar&sourcetype=Dissertations%20&%20Theses>.
43. Yamada, M. & Seki, M. Hydrodynamic filtration for on-chip particle concentration and classification utilizing microfluidics. *Lab. Chip* **5**, 1233–1239 (2005). DOI: 10.1039/D5LC00786K
44. D'Silva, J., Austin, R. H. & Sturm, J. C. Inhibition of clot formation in deterministic lateral displacement arrays for processing large volumes of blood for rare cell capture. *Lab. Chip* **15**, 2240–2247 (2015).
45. Civil, C. I. *et al.* Automated Leukocyte Processing by Microfluidic Deterministic Lateral Displacement. *Cytom. Part J. Int. Soc. Anal. Cytol.* **89**, 1073–1083 (2016).
46. Inglis, D. W., Lord, M. & Nordon, R. E. Scaling deterministic lateral displacement arrays for high throughput and dilution-free enrichment of leukocytes. *J. Micromechanics Microengineering* **21**, 054024 (2011).
47. Campos-González, R. *et al.* Deterministic Lateral Displacement: The Next-Generation CAR T-Cell Processing? *SLAS Technol.* **23**, 338–351 (2018).



Data availability statement

Significant images, data and modelling results have been presented in the manuscript. The importance of protruding obstacles in our device to ‘bump’ large particles is described in Supplementary Information (SI). References 24 and 42 in this article’s reference list are cited in the Supplementary Information (SI). More image data and COMSOL models can be made available to readers. Please contact the authors if required.

Best regards,

Main Author:

Miftahul Jannat Rasna
PhD candidate, Department of Electrical and Computer Engineering, Princeton University, NJ 08542, United States.
Email: mrasna@princeton.edu

Corresponding author:

James C. Sturm
Professor, Department of Electrical and Computer Engineering, Princeton University, NJ 08542, United States.
Email: sturm@princeton.edu

